

High-resolution cryoEM structure determination of soluble proteins after soft-landing ESIBD.

Lukas Eriksson,^{1,2} Tim K. Esser,^{1, a)} Marko Grabarics,^{1,2} Laurence T. Seeley,^{1,2,3} Simon B. Knoblauch,^{1,2} Paul Fremdling,^{2, b)} Thomas Reynolds,⁴ Jani R. Bolla,⁴ Lindsay Baker,^{1,3} and Stephan Rauschenbach^{1,2}

¹⁾*Kavli Institute for Nanoscience Discovery, Dorothy Crowfoot Hodgkin Building, University of Oxford, South Parks Road, Oxford OX1 3QU, UK*

²⁾*Department of Chemistry, University of Oxford, Mansfield Road, Oxford OX1 3TA, UK*

³⁾*Department of Biochemistry, University of Oxford, South Parks Road, Oxford OX1 3QU, UK*

⁴⁾*Department of Biology, University of Oxford, South Parks Road, Oxford OX1 3RB, UK*

(*Electronic mail: stephan.rauschenbach@chem.ox.ac.uk)

(Dated: 31 March 2025)

Soft-landing electrospray ion beam deposition (ESIBD), i.e. the chemically selective, intact deposition of large and complex molecules on surfaces in vacuum, is a well-established sample preparation method for scanning probe microscopy (SPM), where it facilitates the high-resolution imaging of large and complex molecules. Inherited from mass spectrometry, the advantageous properties of ESIBD, chemical purity and selectivity, as well as precise control over the sample environment in vacuum, are also desirable in combination with other analytical methods. Therefore, recently ESIBD has been pursued for the fabrication of samples for electron cryo-microscopy (cryoEM) with proteins introduced into the gas phase via native electrospray ionisation (native ESI). However, the general applicability of this approach and the optimal conditions for an ESIBD-based cryoEM workflow remain unclear. Here, we present instrumentation and methods for a dedicated ESIBD+cryoEM workflow, based on precise control over deposition conditions and sample environment. We establish optimal conditions for gentle deposition of the proteins, for growing homogeneous, ultra-thin, amorphous ice, and for avoiding contamination, which allows for atomic-resolution cryoEM imaging of multiple protein systems. Our results confirm the retention of the protein's native secondary structure and general shape. ESIBD+cryoEM directly links native MS chemical insights with cryoEM's structural precision, offering a versatile platform for structural biology applications.

^{a)}Currently at Thermo Fisher Scientific, De Schakel 2, 5651GH Eindhoven, Netherlands

^{b)}Currently at REELEMENTS GmbH, Wilhelm-Eichler-Straße 34, 01445 Radebeul, Germany

INTRODUCTION

Native mass spectrometry (native MS) is based on the gentle electrospray ionisation (ESI) of proteins and protein complexes and has been shown to retain the analytes' fold and conformation upon transfer into the gas phase.¹⁻³ With a high mass-resolution instrument, detailed chemical information can be obtained, allowing native MS to discern binding, stoichiometry, interaction strength, or heterogeneity of a protein sample.⁴ Information about their three-dimensional can be extracted when native MS is coupled to methods such as ion mobility spectrometry or hydrogen-deuterium exchange.^{5,6} However, the spatial resolution of these approaches is limited compared to the high-resolution conventional methods of structural biology, such as X-ray diffraction or electron cryo-microscopy (cryoEM).

Generally, relating precise chemical information about proteins and their interactions to high-resolution structural information is considered central to many questions in molecular biology, (patho)physiology, and drug discovery.^{2,7} Soft-landing electrospray ion beam deposition (ESIBD),⁸ the gentle deposition of intact molecular ions onto surfaces in vacuum, has attracted attention because of its potential to provide a direct link between the chemical information from native MS and the high-resolution spatial information from cryoEM.⁹⁻¹³ Recently, we demonstrated that the atomic resolution imaging of β -Galactosidase samples prepared using native ESI, mass-selection, gentle deposition, and embedding in a thin ice film is possible.¹⁴ This result showed a general retention of the secondary structure and overall shape of the protein and a small rearrangement of large domains due to the dehydration in the ESI process. However, these experiments revealed several shortcomings of the prototype instrumentation and workflow at the time. Due to a lack of precise control of sample temperature and partial pressure, ice embedding by film growth from the gas phase was inconsistent. The proteins were embedded within polycrystalline ice that varied extensively in thickness and morphology, greatly reducing the collection efficiency of cryoEM data. Further, cryoEM grids were also often contaminated by crystalline ice grown during sample transfer.

These findings prompted two important questions: i) Can this result be generalised for other proteins, and ii) What are the optimal conditions and parameters for a high-resolution ES-IBD+cryoEM workflow. To answer these questions, though, we required novel instrumentation for precise control over a wide range of sample temperatures and atmospheric conditions, to enable controlled embedding of deposited proteins in ice and maintain sample cleanliness throughout the

entire process. This must be implemented while maintaining control over the ion beam, so we built upon our past experience with ESIBD for scanning probe microscopy (SPM),⁸ low energy electron holography (LEEH),^{15,16} and electron microscopy (EM)¹⁷ in the design process.

Here, we show the design of instrumentation which has control over all of these variables, and its application to control the phase, morphology, and thickness of ice layers grown over gently deposited soluble proteins. Enabled by this control, we generalize the results for β -Galactosidase to other soluble proteins, gaining further understanding of the gas-phase structures of soluble proteins. For several protein systems we demonstrate that this workflow can yield high-resolution cryoEM data compatible with the established data analysis pipelines,^{18,19} sufficient for building partial atomic models.

RESULTS

Design and Construction

In ESIBD, a beam of ions is generated by native ESI, processed, and characterised by a mass spectrometer. The ion beam then leaves the mass spectrometer (in our case through an aperture at the exit of a collisional cell) with a well-defined spatial and energy distribution, and from this point onwards is controlled using electrostatic (DC) ion optics. These ion optics (or lenses), shown schematically in Figure 1a-b, have the ability to steer, focus, accelerate, and decelerate the ions, enabling control over deposition location, density, and landing energy. Our ESIBD+cryoEM instrumentation and workflow are implemented on a modified commercial mass spectrometer (Thermo Scientific Q Exactive UHMR instrument), but they can be fitted, in principle, to any ESIBD instrumentation.^{8,12,20–22}

In Figure 1c, all lenses within (and three lenses before) the deposition stage are shown in half-section view. Schematically, they are shown again from the perspective of the ion beam. Sets of three lenses in a row are used as einzel lenses to focus the ion beam. Some lenses are split, allowing for the ion beam to be steered by applying a voltage differential between the resulting lenses.

Sample positions and lenses that function as apertures are connected to picoammeters, which measure the currents of ions colliding with these lenses. By measuring the ion current deposited on a sample position, the amount of ions deposited can be quantified, and measuring the current

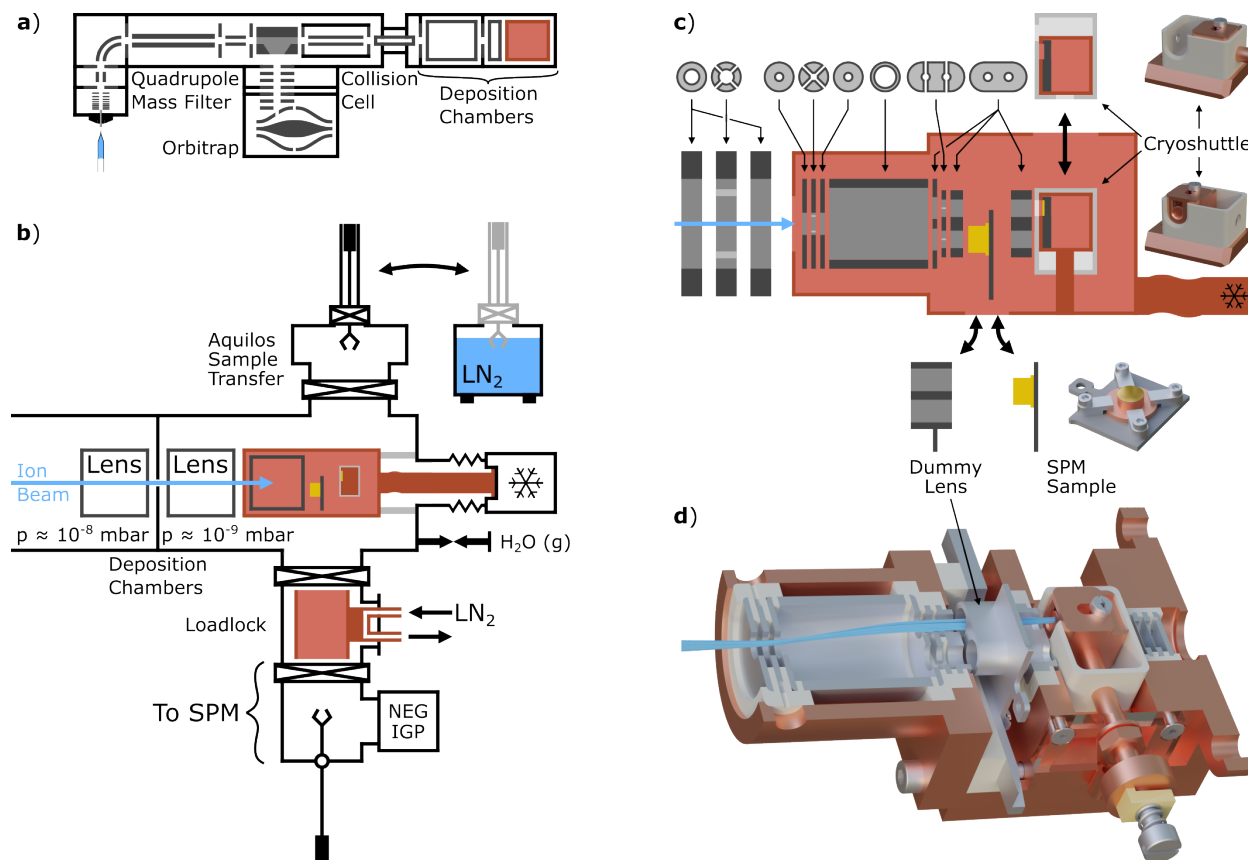


FIG. 1. Instrumentation Overview. **a)** Schematic of the entire deposition instrument. **b)** Schematic of the cryogenic deposition chamber, as well as the sample transfer systems for cryoEM and SPM samples. **c)** Schematic of the cryogenic deposition stage. Cryoshuttle render shown in both deposition mode (open) and transfer mode (shielded). **d)** Section-view rendering of the deposition stage with simulated ion trajectories for deposition onto a cryoEM grid.

on apertures aids in the alignment and focusing of the beam, maximising the efficiency of ion use during deposition.

Within the stage, lenses steer and land the ion beam onto cryoEM grids (held within a cryoshuttle) or SPM crystals (Figure 1c) at defined landing energies from 1 to >100 eV per charge. When depositing on cryoEM grids, the SPM sample is replaced by a custom lens mounted on an SPM sample plate (dubbed the dummy lens) to maintain a well-defined potential for beam transmission (Figure 1d).

To protect the structures of landed proteins from thermal activation,^{13,14} keep the local environment around samples cleaner,²³ enable control over ice growth,²⁴ and limit mobility of molecules on surfaces,²⁵ the stage must be kept at consistent, cryogenic temperatures. A reverse stirling cry-

ocooler (Sunpower Cryotel GTLT, Figure 1b) provides cooling, and a custom mounting assembly limits heat load, while maintaining mechanical rigidity, as shown in Supplementary Figure S1.

A temperature sensor is mounted on a pin which makes good thermal contact to the cryoshuttle when inserted (Figure 1d). This pin also serves as the electrical contact to a power supply that defines the grid potential and thus the landing energy. The deposition stage is fitted with a resistive heating element, which is used in conjunction with the temperature sensor and a PID temperature controller (LakeShore Model 335), regulating the temperature of the shuttle to within <10 mK of a user-defined setpoint between 60 K and 350 K.

To minimize sample contamination, especially when samples are cryogenically cooled, the stage is designed such that sample surfaces do not have direct line of sight to any room temperature surfaces. To keep samples clean during deposition, ultra-high vacuum conditions (UHV, $p < 10^{-9}$ mbar) are necessary. A UHV environment in the deposition chamber is accomplished with two differentially pumped chambers attached to the mass spectrometer (Figure 1a&b). All components of and within the deposition chamber exclusively use UHV-compatible materials, and the chambers are pumped with turbomolecular pumps backed by scroll pumps. When the stage is cryogenically cooled, it functions as a cryopump, decreasing the pressure at the sample which is held within the stage further.²³

To protect cryoEM samples during transfer, a cryoshuttle (compatible with Thermo Scientific Aquilos hardware) is employed. Grids are physically shielded by PEEK shutters during all transfer steps, only being exposed when fully inserted into the deposition stage (see suppl. movie S1). After cryoEM sample preparation, the shuttle is further cooled to 93 K, well below the devitrification temperature of ice to compensate for any warming during transfer²⁴ The shuttle is transferred under static vacuum, followed by a brief transfer through clean nitrogen gas into liquid nitrogen. This process typically takes less than one minute, keeping the grids cold and clean.

SPM samples are transferred under continuous UHV conditions to the microscope, relying on loadlocks, which reach below 2×10^{-8} mbar within an hour of pumping, and a UHV suitcase,²⁶ which remains below 10^{-10} mbar. Three classes of molecules were deposited for proof-of-principle scanning tunneling microscopy (STM) experiments: β -cyclodextrin, a 1135 Da cyclic oligosaccharide; bovine serum albumin (BSA), a 66 kDa protein; and pUC19, a 1.7 MDa plasmid; representative micrographs are shown in Supplementary Figure S2. A new suitcase is in development to allow for the fully cryogenic transfer of samples.

Ice growth on TEM grids

Conventional cryoEM sample preparation by plunge freezing yields proteins embedded in a thin, vitreous layer of ice.²⁷ Critically, the ice must be sufficiently thin (10 nm to 100 nm) for particles to be distinguished in acquired micrographs.²⁸

Proteins deposited by ESIBD are adsorbed on the substrate surface in vacuum, not embedded in ice. Due to the absence of ice, these proteins show very high contrast in micrographs, as seen in Figure 2a. However, 3D reconstructions of ESIBD-prepared proteins show a high-density, unresolved shell at the surface of the protein, making the determination of structural features at the protein surface impossible.¹¹ When ice is grown around ESIBD-prepared proteins, such a high-density shell is not observed in 3D reconstructions, allowing the structure of the entire protein to be determined.¹⁴ Thus, growing ice over deposited proteins is essential for good cryoEM maps.

The optimal ice layer is thin and flat to maximize contrast and increase consistency. It is vitreous, so that proteins are not obscured or disrupted by features such as ice crystal grains and reflections. In our instrument, we grow ice on TEM grids by depositing water vapour onto the surface in a controlled manner. After the deposition of protein molecules is completed, the deposition stage is held at a defined temperature, and a leak-valve to a chamber containing water vapour is opened, raising the partial pressure of water in the chamber to a defined value. By varying the pressure, we vary the flux of water molecules colliding with and condensing onto the surface. After a defined time period, the valve is shut, and excess water vapour is pumped, reducing the partial pressure of water to a negligible amount. By adjusting the duration and pressure of water vapour exposure, we can control the amount of ice grown.

Figure 2 shows a schematic side view, representative micrograph, and inset power spectrum for grids prepared under different conditions. The morphology and phase of the ice deposited can be controlled by varying the pressure of water vapour and the temperature of the sample, as seen in Figure 2b-d. For all, β -Galactosidase was deposited onto TEM grids (Quantifoil) covered with 2 nm amorphous carbon. When ice was grown (Figure 2b-d), the partial pressure of water was brought to 5×10^{-5} mbar for 3 minutes. As the stage acts as a cryopump, the partial pressure of water at the sample surface is about three orders of magnitude lower, based on ice growth rates.²⁴ After ice growth, the stage was cooled to 93 K, and the shuttle was transferred into liquid nitrogen using the Aquilos system, as previously described.¹⁴

Figure 2a shows a grid prepared at cryogenic temperatures, but with no exposure to water

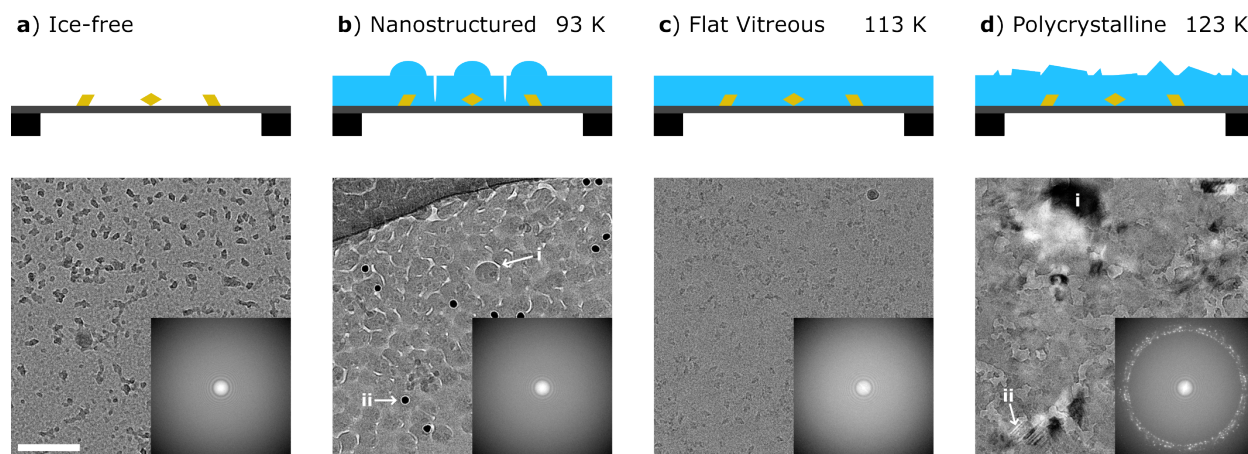


FIG. 2. Control of ice phase and morphology. **a)** Side view schematics, cryoEM micrographs, and inset power spectra of β -Galactosidase deposited without any subsequent ice deposition. Scale bar (same for all micrographs) 100 nm. **b)** Side view schematic, cryoEM micrograph, and inset power spectra of β -Galactosidase deposited with ice grown at 93 K. **c)** Side view schematic, cryoEM micrograph, and inset power spectra of β -Galactosidase deposited with ice grown at 113 K. **d)** Side view schematic, cryoEM micrograph, and inset power spectra of β -Galactosidase deposited with ice grown at 123 K.

vapour. There is very high contrast between the particles and the background, and background noise is indicative of the amorphous carbon layer. Small ice particles are visible on the surface, arising from contamination during sample transfers.

When ice is grown at 93 K, the resulting micrograph has highly variable signal from the grid, with patches of brightness about 5 to 50 nm long (Figure 2bi). The power spectrum without diffraction peaks reveals that the ice is vitreous. The very dark points of contrast (Figure 2bii) are gold fiducials, added to aid with cryo-electron tomography (cryoET). β -Galactosidase particles can be seen, with much lower contrast compared to the ice-free sample. CryoET shows that the deposited ice grows nanostructured columns with rounded tops above the proteins. In some areas, thin, crevasse-like channels of vacuum extend far into the layer of ice, often approaching the underlying carbon support. The proteins are still fully embedded in ice, as shown in Supplementary Figure S3.

When ice is grown at 113 K, the resulting micrograph (Figure 2c) does not feature many bright and dark patches. Particles are visible, with lower contrast when compared to the ice free sample, as expected. The ice is vitreous as evidenced by the power spectrum, and it is 20 nm thick as determined from cryoET (see Supplementary Figure S3).

At 123 K, the ice grown is polycrystalline (Figure 2d). This is evidenced by the patches of bright and dark areas (Figure 2di) and reflections (Figure 2dii) in some regions of the micrograph. The power spectrum clearly shows many diffraction peaks, corresponding to the crystalline domains in the micrograph. Particles are visible, but many are obscured by crystal domains, reducing collection efficiency.

For single particle analysis (SPA), the sample with flat, vitreous ice is ideal. It has high, consistent particle density, and the lack of undesired high-contrast features—coupled with good contrast between the particle and the background—makes particle picking and alignment easier. While particle contrast is not as high as in ice-free samples, resulting 3D reconstructions are free from high-density shells on the surface of the protein. With precise control over the pressure of water vapour, stage temperature, growth time, and sample transfer to liquid nitrogen, samples can now be generated with consistently optimal ice embedding.

ESIBD+cryoEM workflow for soluble proteins

Using the procedure for deposition and consistent ice growth, we prepared samples of different soluble protein complexes to benchmark our approach: β -Galactosidase, a homotetrameric enzyme; Glutamate Dehydrogenase (GDH), a homohexameric enzyme; Ribulose-1,5-bisphosphate carboxylase/oxygenase (RuBisCo), a hetero-16-meric enzyme made up of 8 large subunits and 8 small subunits; and GroEL, a homo-14-meric chaperonin. Solutions of the proteins were prepared at 1 to 10 μ M concentration in 200 mM ammonium acetate (pH 6.9) then loaded into gold-coated nano-electrospray ionization emitters pulled from borosilicate glass capillaries, as standard for native MS.¹¹

In native MS, steps are often taken to narrow peak widths by increasing desolvation and activation of the protein complex, removing adducts such as water molecules and salts.^{1,4} This can be done in several places throughout the mass spectrometer. The capillary which transfers the electrospray droplets into vacuum can be heated up to 300°C to increase evaporation of water. In the source, voltage gradients can be increased to accelerate ions faster, increasing the energy of collisions with the surrounding buffer gas molecules, and trapped, increasing the duration within the source, increasing the number of collisions with buffer gas molecules. Similarly, ions can be accelerated and collisionally activated in a collision cell.

For deposition, we set the capillary temperature to 50°C and apply no desolvation voltage, in-

source trapping, or activation in the collision cell. This results in wide peaks (50-100 Th FWHM, Figure 3) compared to many reported native mass spectra,^{24,29} due to the undefined stoichiometry of residual water and other adducts. These gentle spray conditions are intended to minimize the thermal and collisional activation of the proteins, a key aspect of our workflow.

Once spray conditions are set, we first record the mass spectra of the proteins without any mass selection; see Supplementary Figure S4. The desired species are then selected with the quadrupole mass filter (Figure 1a), excluding impurities and undesired oligomers. During deposition the ions are guided through the collision cell, where a gentle voltage gradient and high pressure of nitrogen gas lead to many low-energy ion-nitrogen collisions, thermalizing the ions and narrowing the energy distribution of the ion beam.³⁰

After this, the ion beam enters our custom, high vacuum instrumentation, where there are no more collisions with gas molecules. At this point, beam energy is defined and will be conserved until deposition; in our setup, soluble protein ion beams are typically centered in energy around -7 eV per charge (with respect to electrical ground), with a FWHM of 1 to 1.5 eV per charge. The ions are then directed to the grid which is held at a temperature below 120 K. The electrical potential of the grid is typically set to -8.5 V for very gentle landing (<2 eV per charge), and the quantity deposited is monitored by integrating the deposition current over time. We landed 11 pAh of β -Galactosidase, 15 pAh of GDH and GroEL, and 10 pAh of RuBisCo; this results in roughly 1 mm² of the grid having optimal particle density for data collection. An optimal density maximizes the number of particles per micrograph without particles being so close together that they hamper alignment and particle picking. Ideally, particles will be spaced approximately one particles length away from all nearest neighbours.

After protein deposition, the sample temperature was adjusted to 113 K and ice was grown for 3 minutes at 5×10^{-5} mbar. The samples were then cooled to 93 K, 40 K below devitrification temperature to keep samples vitreous during transfer when they are not actively cooled.²⁴ The transfer consists of purging the loadlock with clean nitrogen gas before inserting the entire cryoshuttle into liquid nitrogen using the Aquilos system as previously described.¹⁴ From here, the samples can be handled identically as samples prepared by plunge freezing: stored in liquid nitrogen until imaging, imaged using typical microscope settings, and the resulting data processed with standard workflows.^{18,19}

With control over activation through the mass spectrometer, thermalization of the ions in the collision cell, gentle landing energies, and consistent ice growth, the samples are suitable for

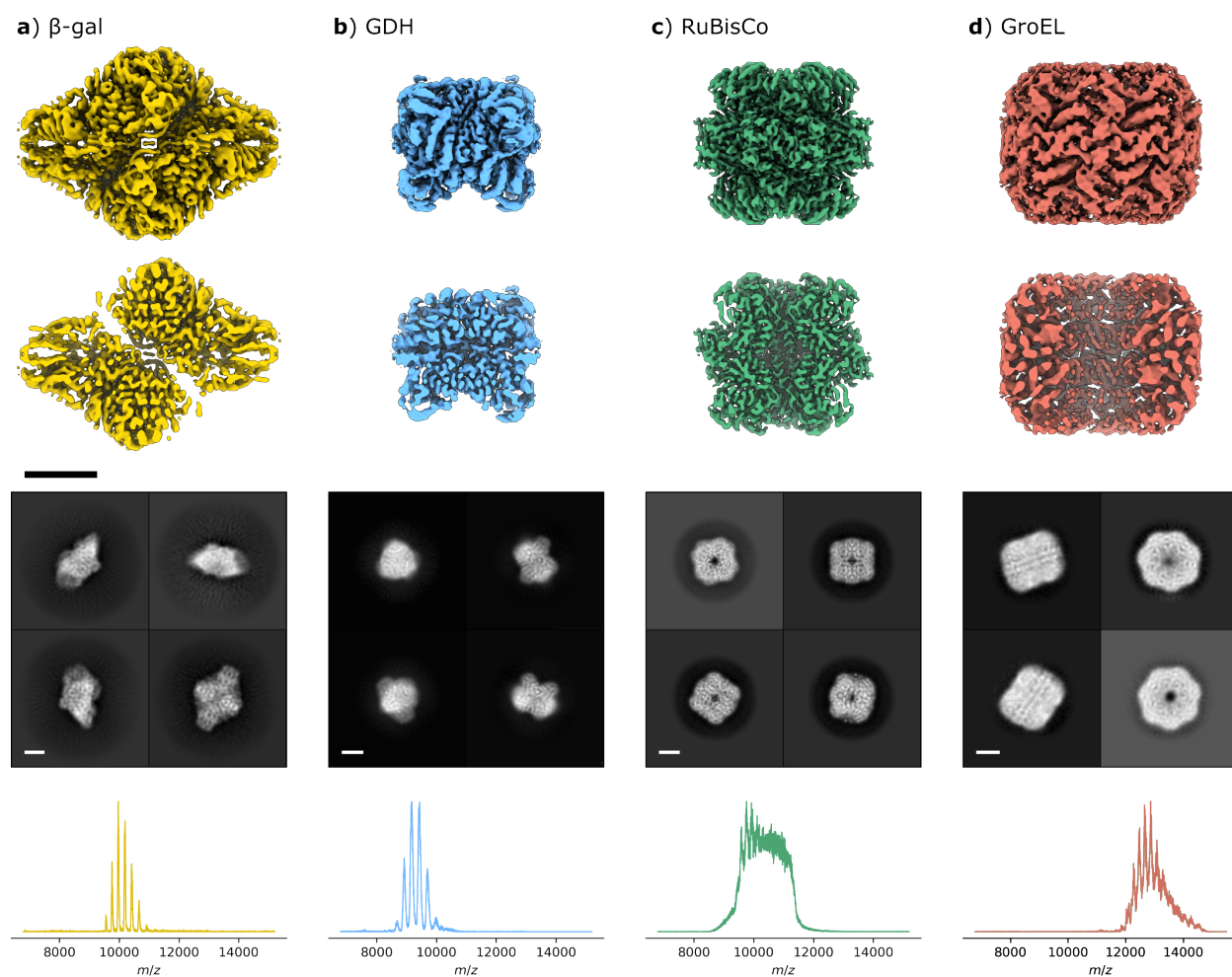


FIG. 3. **ESIBD-prepared soluble protein maps.** CryoEM density maps (scale bar 5 nm), selected 2D classes (scale bars 5 nm) and deposited mass spectra for beta-gal (**a**), GDH (**b**), RuBisCo (**c**), and GroEL (**d**).

structural analysis with cryoEM. The consensus 3D reconstructions, with symmetry (D2, D3, D4, and D7, respectively) imposed, are shown in Figure 3, along with selected 2D classes and mass spectra of the mass-filtered ion beam selected for deposition.

For β -Galactosidase, charge states 43+ to 48+ were deposited, with mass filtration in the quadrupole effectively isolating this range, as seen in the mass spectrum in Figure 3a. 2D classes indicate several different particle orientations on the grid, essential for good 3D reconstruction.³¹ 3D reconstruction with D2 symmetry applied yields a map with a resolution of 3.09 Å.

For GDH, charge states 33+ to 38+ were deposited, with mass filtration effectively isolating this range and well-defined peaks, as seen in Figure 3b. 2D classes indicate multiple particle orientations on the grid, and 3D reconstruction yields a 2.54 Å map with D3 symmetry imposed.

With RuBisCo, the mass spectrum consists of several distinguishable peaks at lower mass-to-charge values (charge states 55+ to 58+), which blur into unresolved intensity above 10500 Th (Figure 3c). With activation, sharp peaks emerge by reducing the number of adducts, confirming the chemical purity of the beam. However, no activation was used for deposition. 2D classes show several orientations, and 3D reconstruction with D4 symmetry results in a 2.58 Å map.

GroEL, the heaviest of the four protein complexes, shows resolved peaks in the mass spectrum, of which charge states from 60+ to 67+ were deposited. 2D classification yields two predominant orientations, a view down the central C7 symmetry axis, and a perpendicular side view. Within these two general orientations, slight variations in tilt are observed. 3D reconstruction results in a 4.8 Å map with D7 symmetry.

All proteins studied here, which vary in size, expression organism, and oligomeric stoichiometry, show 2D classes with characteristic features of α -helices and β -sheets, and the reconstructed 3D maps are high-resolution, suitable for building partial atomic models.

Structural analysis of ESIBD-prepared proteins

The maps obtained from ESIBD+cryoEM show several consistent trends beyond being suitable for building atomic models. Firstly, local resolution is lower at protein surfaces: This was observed in our proof-of-principle experiments on β -Galactosidase and holds true for all maps generated for soluble proteins prepared by ESIBD (Figure 4). More precisely, regions of the protein with greater exposure to solvent in their native state show more disorder in maps generated by ESIBD+cryoEM. These are regions of the protein where a greater proportion of their local interactions—through hydrogen bonds, polar/ionic interactions, and Van der Waals interactions—are with solvent molecules. Upon ESI and subsequent dehydration, these interactions are largely removed; additionally, the screening provided by liquid water is removed, increasing the strength of Coulombic interactions such as hydrogen bonds and dipole-dipole interactions. The dehydrated protein is no longer at an energetic minimum, most notably in previously solvent-exposed regions, and therefore will rearrange to form new interactions where kinetically feasible. In vacuum, these new interactions must be intramolecular.

Secondly, there is some level of compaction observed when compared to maps reconstructed from conventional cryoEM workflows, often enabled by subunit reorientation. This was previously observed for β -Galactosidase, and again is seen for all ESIBD-prepared soluble protein maps.

This compaction and reorientation, however, varies between different proteins. The compaction of GroEL is very pronounced, as illustrated by the comparison of a PBD model (5W0S) to our ISOLDE-relaxed model in Figure 4f. The analogous comparison for RuBisCo (Figure 4d), on the other hand, shows almost no compaction.

Compaction and subunit reorientation also arises from the removal of favourable protein-solvent interactions and the decreased screening from bulk water, making cavities (as seen in the centre of β -Galactosidase and between the equatorial and apical domains in each groEL monomeric subunit³²) thermodynamically less favourable. Thus, surrounding domains will reorient to replace the lost protein-solvent interactions with protein-protein interactions where kinetically accessible, resulting in a net compression of the protein.

As previously reported, the ESIBD structure of β -Galactosidase shows large parts of the secondary and tertiary structure retained from solution. Dehydration-induced subunit reorientation compacts the protein in the gas phase.¹⁴ Here, we will focus on the ESIBD structures of GDH, RuBisCo, and GroEL. Refer to Supplementary Figure S5 for further details of the β -Galactosidase map, which reproduces our previously reported behaviour.

Figure 4a shows the structural details of GDH. The local resolution in the core ranges from 2.2 to 2.9 Å, with resolution of the surface extending the range up to 5.8 Å. This generally matches the behaviour seen in β -Galactosidase very well, with the most solvent-exposed sections being at the lowest resolution. Interestingly, with D3 symmetry imposed, one alpha helix per subunit (residues 398 to 425 on PDB model 3JCZ) which protrudes along the C3 axis of symmetry, away from the rest of the globular protein, is not resolved.

We performed further heterogeneous refinement (shown in detail in Supplementary Figure S6) with no symmetry applied, yielding a subset of particles which reconstructed a map in which the collapse of one set of 3 alpha helices is observed (Figure 4b). These alpha helices are the most solvent-exposed region of GDH. Upon transfer into the gas phase, the majority of local interactions are removed, with only the two neighbouring alpha helices offering any stabilizing interactions. Consequently, each set of 3 alpha helices heterogeneously collapses onto the nearby protein surface, forming intramolecular interactions that were previously occupied by water.

The map generated for RuBisCo, shown in Figure 4c, has local resolution in the core ranging from 2.3 to 2.9 Å, very similar to GDH and β -Galactosidase. There are two notable differences when comparing RuBisCo to GDH and β -Galactosidase. Firstly, local resolution of the surface is better (4.1 Å) than β -Galactosidase (5.1 Å) or GDH (5.8 Å), as shown in Figure 4c. Additionally,

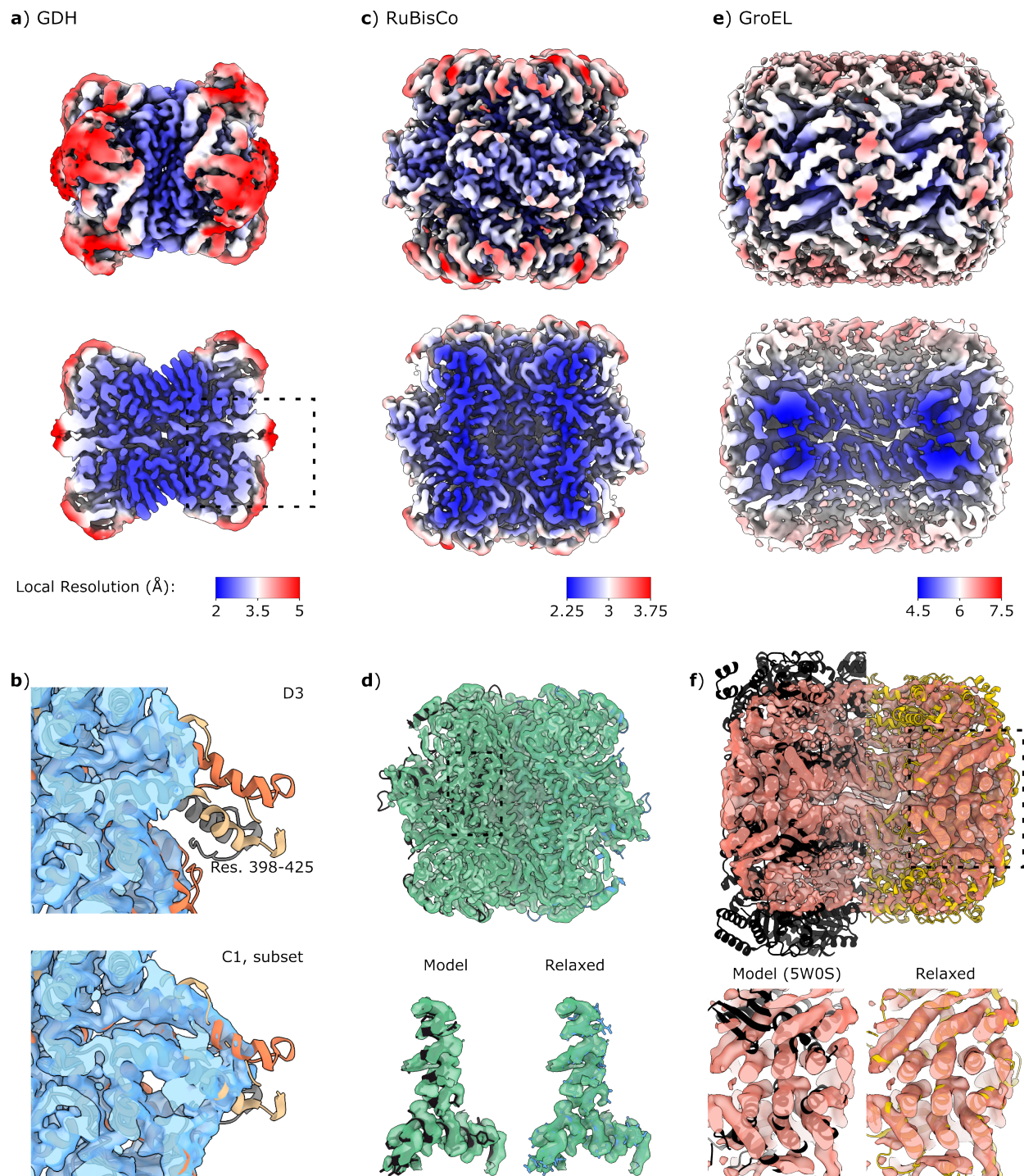


FIG. 4. Structural details of ESIBD-prepared soluble proteins. a) Local resolution map of GDH (FSC threshold 0.5). **b)** Zoomed view around residues 398-425, showing how they are resolved in a C1 reconstruction of a subset of GDH particles. **c)** RuBisCo local resolution map and **d)** comparison of plunge-frozen model with ISOLDE-relaxed model. **e)** GroEL local resolution map and **f)** comparison of plunge-frozen model (PDB entry 5W0S) with ISOLDE-relaxed model.

RuBisCo hardly compacts (only 1.5% across its width) and its subunits reorient less than the other proteins (see Figure 4d). Two alpha helices from the core were selected to illustrate the slight shift due to ESI/dehydration-induced compaction, as well as the high resolution achieved.

The ESIBD GroEL map (Figure 4e) shows lower resolution than those of β -Galactosidase, GDH, and RuBisCo. Following the same behaviour, local resolution in the core is better (4.4 to 5.6 Å) than at the surface (up to 8.4 Å). GroEL also shows the most dramatic compaction of all proteins we have deposited, with a 24% reduction in height (along the central cavity/C7 axis) but almost no reduction in overall particle width (perpendicular to the C7 axis), when compared to plunge frozen controls.³³ This compaction can be clearly seen in Figure 4f, where we compare a conventional cryoEM model³⁴ to our model, which was relaxed into our map using ISOLDE.³⁵ Smaller water cavities (excluding the central pore) are absent from this map, and the two heptameric rings twist by 5° with respect to each other around the central C7 axis, enabling tighter compaction. This compaction, as with other gas-phase structures, forms protein-protein interactions that had previously been occupied by protein-water interactions.

DISCUSSION

Here, we present a workflow for high resolution structure determination of soluble proteins prepared using ESIBD+cryoEM, enabled by extensive control of the protein and its environment throughout the ESIBD process. UHV conditions in the deposition stage and clean sample transfers minimize the contamination of samples. Minimizing activation and thermalizing in the mass spectrometer lowers the energy of the ion beam, reducing the number of kinetically accessible rearrangements individual protein complexes can undergo while in the gas-phase. Low landing energies (<2 eV per charge) and cryogenic sample temperatures also limit the number of rearrangements kinetically accessible to protein complexes during and after landing. Mass selection enables greater chemical selectivity, offering many potential areas of future investigation, such as the gas-phase enrichment of low-abundance species for deposition. This has potential to be very useful applied to proteins which are difficult to purify using traditional biochemical methods or for low-abundance species in equilibrium with other, undesired species, for example pulling out the desired complexes of protein-protein/protein-drug interactions or individual species from a polydisperse system. We also aim to generalize our ESIBD+cryoEM beyond soluble proteins by investigating the gas-phase structure of membrane proteins.^{36,37}

Our instrumentation also enables the consistent growth of thin, vitreous ice around deposited proteins, by precisely controlling sample temperature during ice growth, the partial pressure of water, and the period of ice growth. After the growth of ideal ice layers, high-resolution maps of soluble proteins can be reconstructed with standard cryoEM imaging and single particle analysis workflows.

The combination of mass selection, clean environments, control over activation during ESIBD, and embedding of deposited protein complexes in ice results in consistently high-resolution (<5 Å) structures of soluble proteins prepared and imaged with ESIBD+cryoEM. This provides greater insight into the gas-phase structure of proteins and protein complexes, as well as the factors that contribute to the stability (or instability) of native configurations in ESIBD processes, and by extension, in native mass spectrometry.

Solvent exposure is a dominant factor for the gas-phase stability of protein regions. Highly solvent-exposed regions of proteins have a greater thermodynamic drive to reorient, forming protein-protein interactions to replace protein-solvent interactions lost to dehydration. The strength and anisotropy of interactions which remain after dehydration are augmented by the lack of shielding which water provides in solution. These factors combine to increase the observed heterogeneity, and in some cases collapse, of solvent-exposed regions of soluble proteins in ESIBD+cryoEM.

METHODS

Solution Preparation

GDH (G7882) was purchased from Sigma-Aldrich; the lyophilized powder was reconstituted in 200 mM ammonium acetate (pH 6.9) to a final concentration of 20 μ M. β -Galactosidase,¹⁴ GroEL¹¹, and RuBisCo³⁸ were prepared as previously described.

All proteins were desalted by eluting through two P6 buffer exchange columns (7326222, Bio-Rad), equilibrated with 200 mM ammonium acetate (pH 6.9). They were then diluted in 200 mM ammonium acetate (pH 6.9) to reach the concentration used for native MS: 10 μ M (β -Galactosidase and GDH), 5 mg / mL (RuBisCo), and 5 μ M (GroEL). Buffer exchange was always done on the day of deposition.

Native MS

Native MS was performed as previously described.¹¹ All spectra shown in figures are what were selected for deposition.

Preparation of ESIBD cryoEM samples

Mesh size 400 copper TEM grids with 3 nm amorphous carbon on a lacey carbon film (AGS187-4; Agar Scientific) and 2 nm amorphous carbon on a R2/1 holey carbon film (C2-C15nCu40-01; Quantifoil) were purchased. Gold TEM grids with mesh size 300 and 2 nm amorphous carbon on a R1.2/1.3 holey carbon film (C2-A14nAu30-50) were purchased from Quantifoil.

Grids were clipped then plasma cleaned for 30 seconds before deposition. The clipped, cleaned grid was loaded into the cryoshuttle, where it is held in position by springs. The top can then be closed, isolating the grid from the atmosphere during transfer. The shuttle is loaded partially into the stage before deposition, so that there is good thermal contact, but the grid is not yet exposed to atmosphere; this keeps the grid cleaner when ice is already condensed on the stage, as insertion of the room temperature cryoshuttle heats up the stage, sublimating some water. After 5 minutes of temperature equilibration, the cryoshuttle is fully inserted and ready for deposition with the grid exposed.

Deposition methodology is described in the workflow section above, then transfer into liquid nitrogen is performed as previously described.¹⁴

Movie acquisition and processing

All micrographs were collected using a Thermo Scientific Krios 300 kV cryo-TEM equipped with a BioQuantum energy filter operated at a slit width of 20 eV and a K3 direct electron detector (both Gatan), located at the COSMIC cryoEM facility. Automated data acquisition was controlled using EPU software (Thermo Scientific). All movies were recorded in the tif format, using a range of defocus settings between -1 and -3 μm , an exposure of $40 e^-/\text{\AA}^2$, and a magnification of 105,000 corresponding to a pixel size of 0.83 \AA .

Data were processed using cryoSPARC.¹⁸ After running Patch Motion Corr. and Patch CTF jobs, particles were picked using template picking, based on templates from manual picking, and

extracted. After multiple rounds of 2D and 3D classification, final maps were produced using local refinement (β -Galactosidase, GDH, RuBisCo) or non-uniform refinement (GroEL), based on ab initio initial volumes generated from our data. This was followed by local resolution estimation. Symmetry was imposed in non-uniform refinement and local refinement, but using C1 symmetry resulted in only slightly lower resolution. Figures and movies of the resulting 3D EM density maps were generated using ChimeraX.³⁹ Further movie acquisition and processing details are specified in Figures S5 to S8 and Table S2.

Tomogram acquisition and processing

Tomographic data were acquired with the previously described Titan Krios. Tilt series were collected with SerialEM⁴⁰ using dose-symmetric acquisition ($\pm 60^\circ$) with 3° tilt increments at a magnification of 81800 and pixel size of 1.106 Å/pixel. Image frames (0.24 s exposure/frame) were collected at a dose rate of 11.3 e-/pixel/s at a target defocus of -4 μm . Tomograms were reconstructed using IMOD.⁴¹

Preparation of ESIBD STM samples

Single crystals of gold and copper were obtained from Mateck GmbH, with the (111) and (100) faces polished, respectively. To achieve a clean, atomically-flat surface, 3 cycles of sputtering (Ar, $p = 10^{-5}$ mbar, 1 kV DC electron gun) and annealing (with resistive heater, to 800 K for 5 mins) were used. Samples were then transferred into a UHV vacuum suitcase, removed from the SPM by venting the loadlock, and carried to the ESIBD instrument; the loadlock was pumped to 2×10^{-8} mbar, and the sample was transferred into the deposition stage.

β -Cyclodextrin (C4767), purchased from Sigma Aldrich, was dissolved into a 50:50 v:v solution of deionised water (MilliQ):HPLC grade methanol to yield a final concentration of 10 μM . Bovine serum albumin (A0281) was purchased from Sigma Aldrich, then 9 mg were dissolved into 24.75 mL deionised (MilliQ) water, 24.75 mL HPLC grade acetonitrile, and 0.5 mL HPLC grade formic acid. The plasmid pUC19 (SD0061), in a 10 mM Tris-HCl and 1 mM EDTA buffer, was purchased from Thermo Scientific. This was then diluted in a solution of 66% v/v ACN (in deionised (MilliQ) water) to a final plasmid concentration of 0.3 nM.

Solution was added to gold-coated (with a sputter coater: 108A/SE, Cressington) nano-

electrospray ionization emitters pulled from borosilicate glass capillaries (30-0042, Harvard Bioscience) using a pipette puller (P-1000, Sutter Instrument). Normal MS settings were used, with lower HCD cell pressure for thermalizing the ion beam. First, a mass spectrum without mass selection was obtained, and then mass selection was used to isolate and deposit only the desired species. For β -cyclodextrin, individual adducts (specifically just the Na^+ adduct) were selected for deposition. Sample potential was set to -9 V for a landing energy of 2 eV per charge. Charge accumulated was monitored to measure the amount of ions deposited: 2 pAh for β -cyclodextrin, 16 pAh for bovine serum albumin, and 10 pAh for pUC19.

After deposition, the sample was transferred into the vacuum suitcase, the loadlock was vented, the suitcase was carried to the SPM, and the loadlock on the SPM was pumped to 2×10^{-8} mbar. The sample was then transferred into the microscope head, allowed to stabilize in temperature (9.3 to 9.7 K). Samples were imaged using scanning tunnelling microscopy in constant current mode with tunnelling currents between 1 and 100 pA and images were processed in Gwyddion.⁴²

ACKNOWLEDGMENTS

We wish to acknowledge support from Thermo Fisher Scientific who provided the Q Exactive UHMR mass spectrometer and the Aquilos sample transfer system within the framework of a technology alliance partnership. We thank E. Silvester for her help with tomogram acquisition. We wish to acknowledge support from the COSMIC microscope facility, especially from R. Matadeen.

Funding

This research was supported by the BBSRC (BB/W017024/1, BB/V019694/1) and the EPSRC (EP/V051474/1). L.T.S. would like to thank the Wellcome Trust (218482/Z/19/Z; Wellcome-funded 4 year PhD program in Cellular Structural Biology). Research in the J.R.B. laboratory is supported by the Royal Society through the University Research Fellowship grant (URF/R1/211567).

Author Contributions

L.E., T.K.E., and S.R. conceived the experiments. L.E., T.K.E., P.F., and S.R. designed and constructed the custom deposition hardware. T.R. and J.R.B. expressed and purified RuBisCo.

L.E., T.K.E., and S.B.K. prepared solutions, performed native ESIBD, imaged, and performed data analysis for cryoEM samples. L.T.S. and L.B. collected and built all tomography data. L.E. and M.G. prepared solutions, performed ESIBD, and imaged STM samples. L.E. and S.R. drafted the manuscript. All authors contributed to the interpretation of results and reviewed the manuscript.

Competing Interests

T.K.E. is an employee of Thermo Fisher Scientific, manufacturer of the Q Exactive UHMR, Aquilos, Arctica, and Krios instruments used in this research.

**Supplementary Materials for
High-resolution cryoEM structure determination of soluble proteins after
soft-landing ESIBD.**

Lukas Eriksson *et al.*

Corresponding Author: stephan.rauschenbach@chem.ox.ac.uk

This PDF file includes

Figs. S1 to S7

Tables S1 and S2

Other Supplementary Materials for this manuscript include the following:

Movie S1

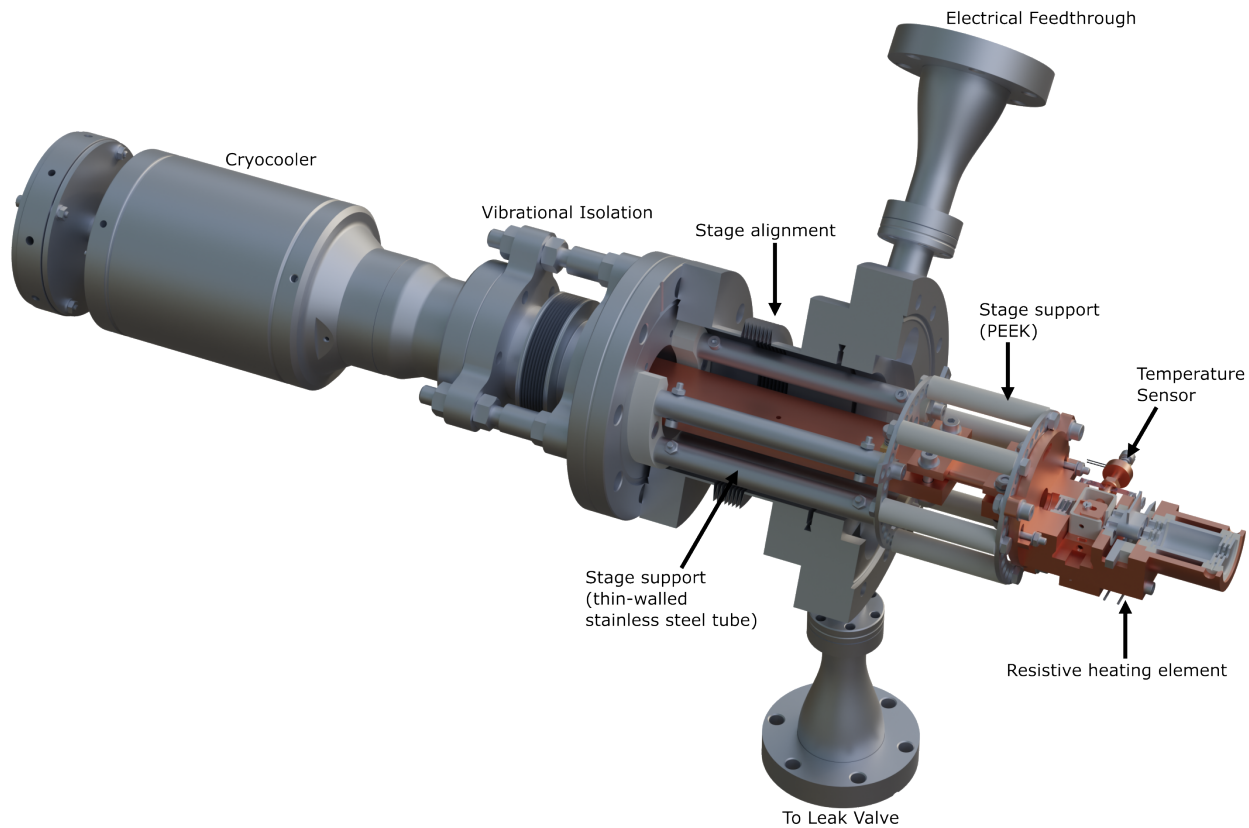


FIG. S1. **Deposition stage, support, and cryocooler** shown in half-section view of mounting flange. Key components are labelled.

TABLE S1. **CryoEM data collection settings for ice micrographs and cryoET.**

	Ice Micrographs	CryoET
Data collection		
Microscope	Talos Arctica	Krios G3
Magnification	105,000	81,800
Voltage (kV)	200	300
Electron exposure ($e^-/\text{\AA}^2$)	40	2.22 per frame (90.9 total)
Defocus (μm)	-3	-4
Pixel size (\AA)	1.17	1.106

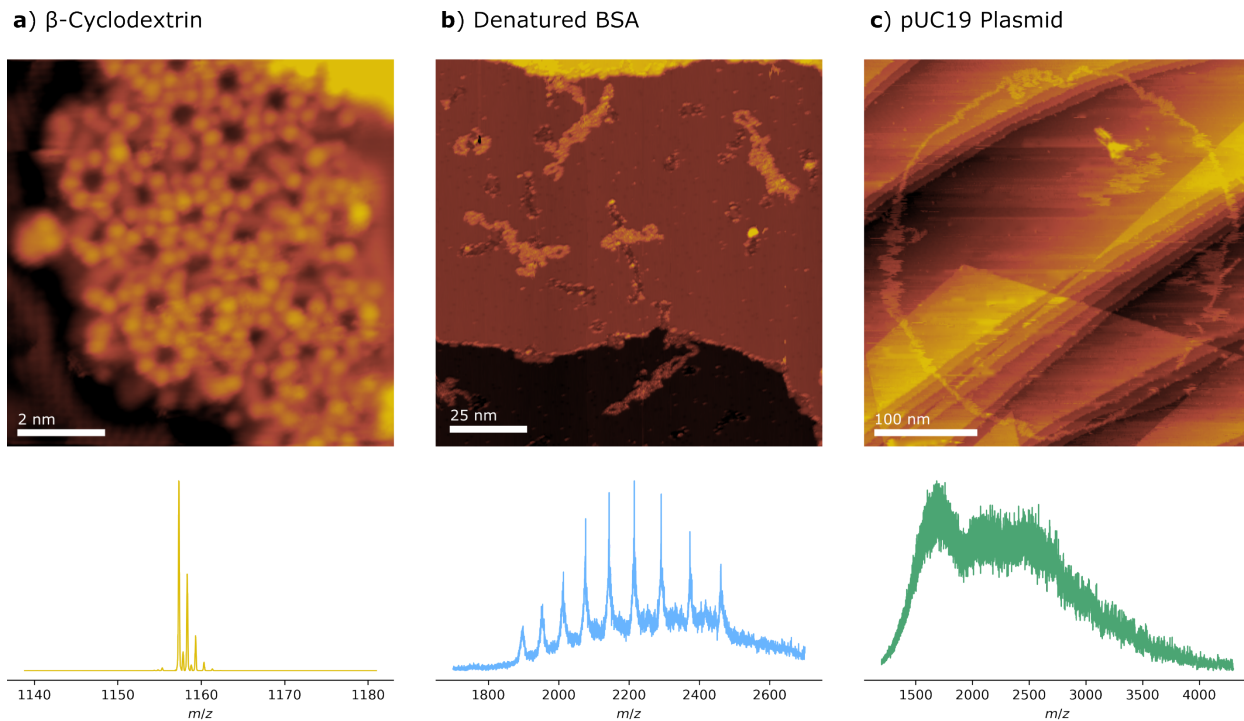


FIG. S2. **ESIBD-prepared STM samples.** Representative micrographs and deposited mass spectra for (a) β -cyclodextrin on Au(111), b) denatured bovine serum albumin on Cu(100), and c) pUC19, a plasmid, on Au(111).

TABLE S2. **Cryo-EM data collection, refinement, and validation statistics.**

	ESIBD β -galactosidase	ESIBD GDH	ESIBD RuBisCo	ESIBD GroEL
Data collection and processing				
Microscope	Krios G3	Krios G3	Krios G3	Krios G3
Magnification	105,000	105,000	105,000	105,000
Voltage (kV)	300	300	300	300
Electron exposure ($e^-/\text{\AA}^2$)	40	40	40	40
Defocus range (μm)	-1.5 to -3	-1 to -2.5	-1.5 to -3	-1 to -2.5
Pixel size (\AA)	0.83	0.83	0.83	0.83
Symmetry imposed	D2	D3	D4	D7
Initial particle images (no.)	668,677	570,602	227,522	327,080
Final particle images (no.)	576,057	474,349	224,331	75,264
Map resolution (\AA)	3.09	2.54	2.58	4.80
FSC threshold	0.143	0.143	0.143	0.143
Map resolution range (\AA)	1.9 to 4.5 (FSC 0.143) 2.58 to 5.1 (FSC 0.5)	1.8 to 5.3 (FSC 0.143) 2.25 to 5.8 (FSC 0.5)	1.8 to 3.4 (FSC 0.143) 2.3 to 4.1 (FSC 0.5)	3.2 to 6.5 (FSC 0.143) 4.45 to 8.4 (FSC 0.5)

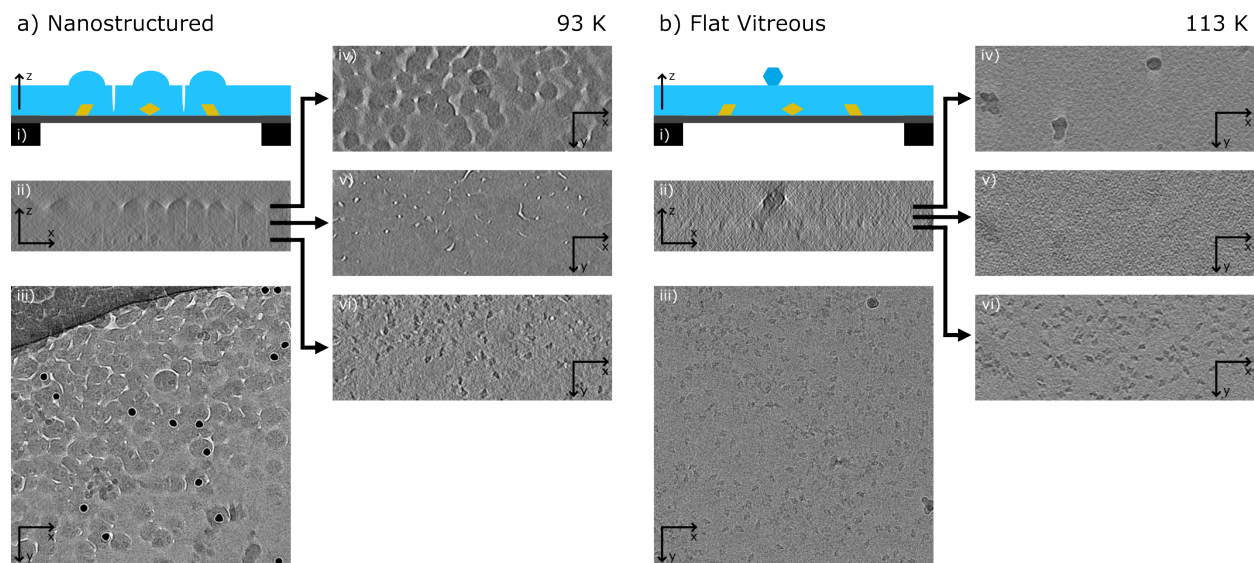


FIG. S3. **Cryo-electron tomography of nanostructured and flat vitreous ice samples.** **a)** Nanostructured ice, grown at 93 K shows columns of ice with rounded tops grown, as shown in a schematic side view in **i**. **ii)** shows a slice through the tomogram in the xz -plane, the same as the schematic side view. Particles can be seen towards the bottom as darker patches. Bright, vertical lines show the channels of vacuum that are formed during nanostructured ice growth, and the rounded tops of the nanostructures can be seen in the top half. **iii)** shows a top-view micrograph. Slices in the xy -plane are shown through the tops of the nanostructured growths (**iv**), through the ice layer, interrupted only by channels of vacuum (**v**), and through the proteins (**vi**). **b)** shows an analogous schematic, micrograph, and slices for a sample with flat, vitreous ice grown at 113 K. In the schematic (**i**), a crystal of ice is shown, which was picked up during handling under liquid nitrogen. This crystal (and others) were used to find the thickness of deposited ice layers, as the flat, vitreous ice was difficult to differentiate from vacuum in cryoET. This is seen in (**ii**), where particles can be seen as small, dark patches, then a region with a lack of features besides noise, and then the aforementioned crystal of ice. Slices are shown through the bottom of ice crystals (**iv**), through the layer of ice (**v**), and through the particles (**vi**). A micrograph (**iii**) is also shown.

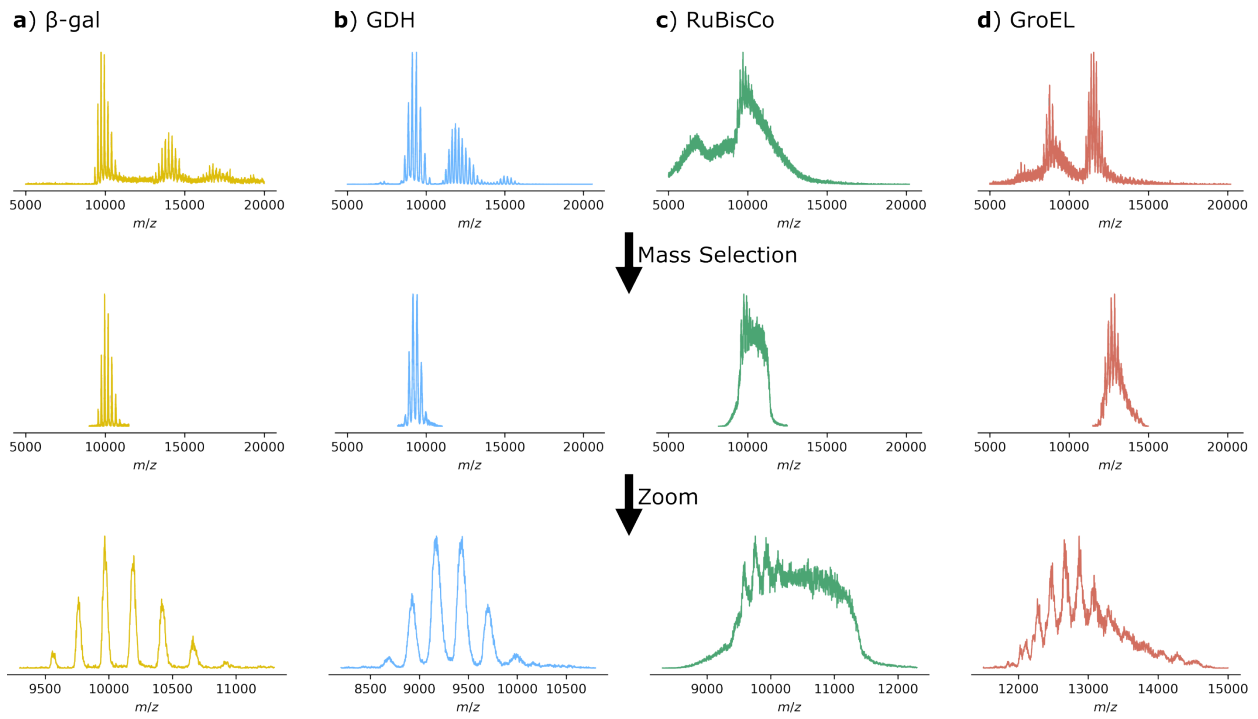


FIG. S4. Mass Filtration of proteins. **a)** Selection of β -gal tetramer. **b)** Selection of GDH hexamer. **c)** Selection of RuBisCo 16-mer. **d)** Selection of GroEL 14-mer.

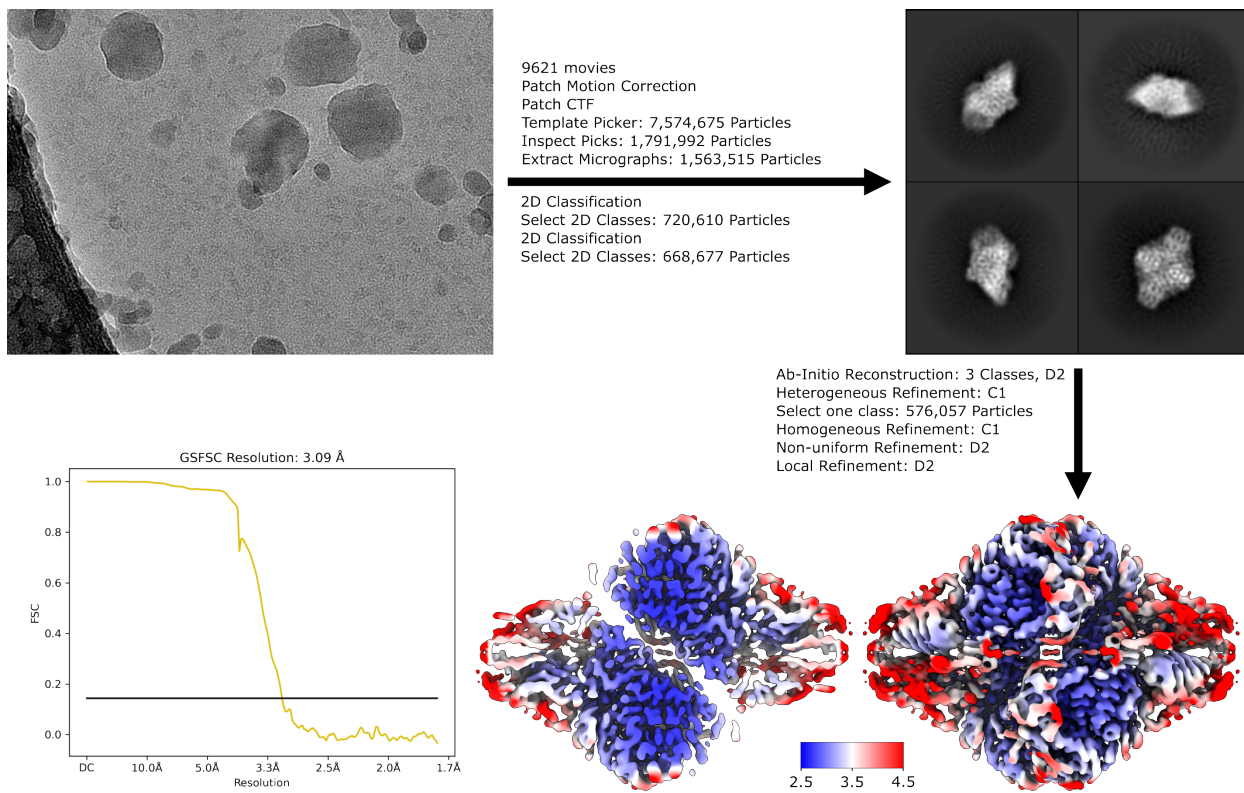


FIG. S5. β -galactosidase processing pipeline and local resolution map.

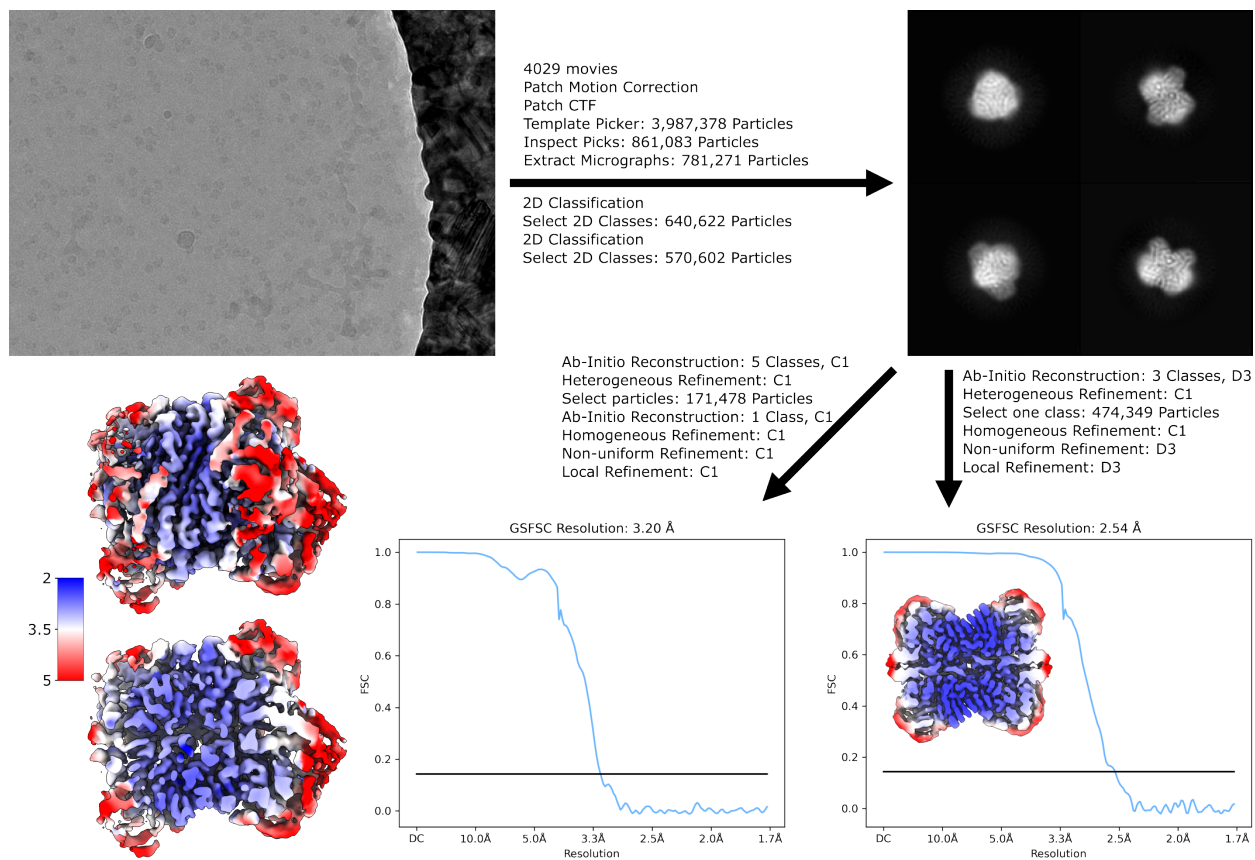


FIG. S6. Glutamate Dehydrogenase (GDH) processing pipeline and local resolution map of C1 subset.

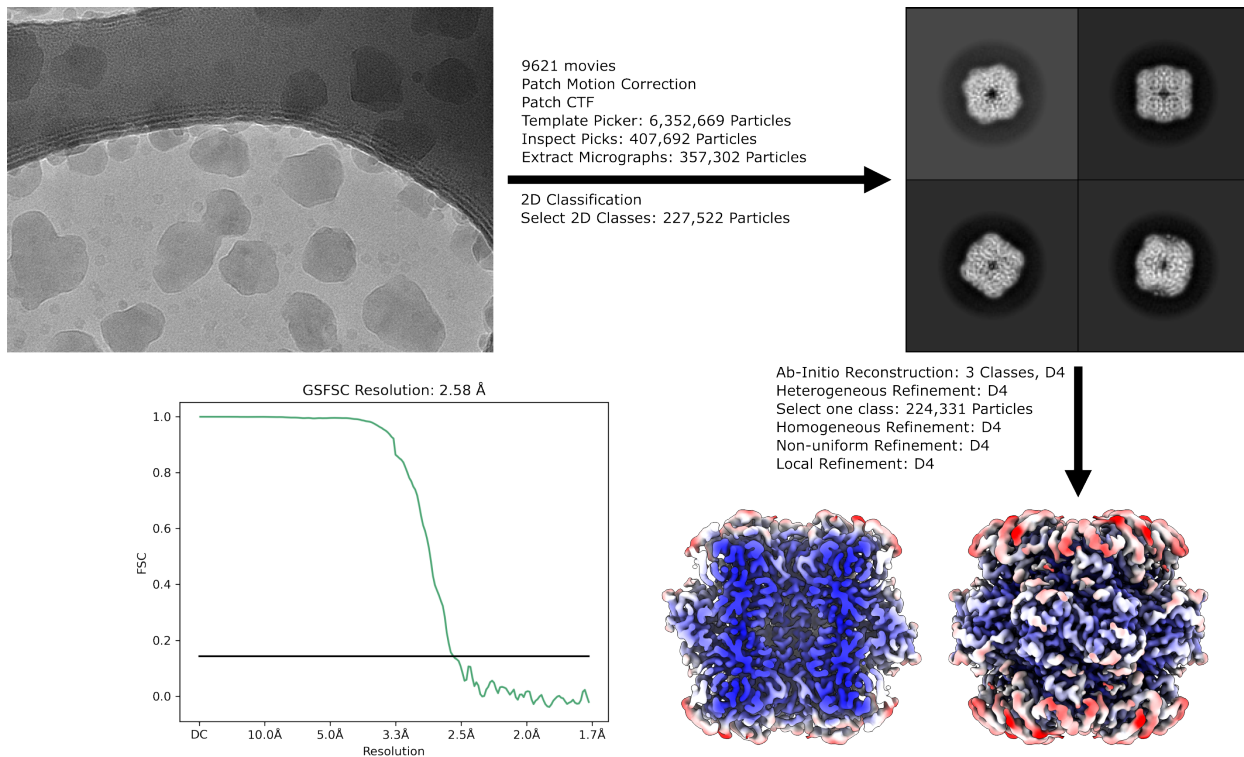


FIG. S7. RuBisCo processing pipeline.

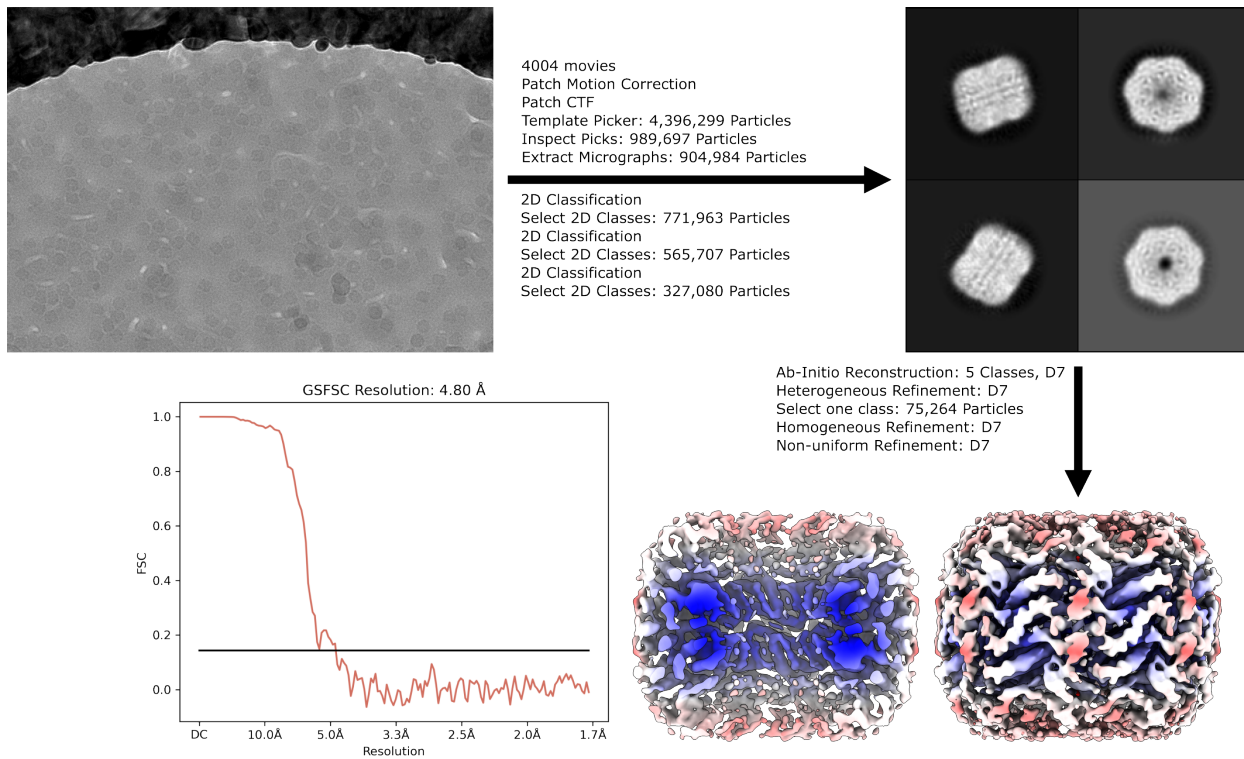


FIG. S8. GroEL processing pipeline.

REFERENCES

- ¹A. J. R. Heck, “Native mass spectrometry: a bridge between interactomics and structural biology.” *Nature methods* **5**, 927–33 (2008).
- ²I. Liko, T. M. Allison, J. T. S. Hopper, and C. V. Robinson, “Mass spectrometry guided structural biology,” *Current Opinion in Structural Biology* **40**, 136–144 (2016).
- ³S. Tamara, M. A. den Boer, and A. J. R. Heck, “High-resolution native mass spectrometry,” *Chemical Reviews* **122**, 7269–7326 (2022).
- ⁴J. Gault, I. Liko, M. Landreh, D. Shutin, J. R. Bolla, D. Jefferies, M. Agasid, H.-Y. Yen, M. J. G. W. Ladds, D. P. Lane, S. Khalid, C. Mullen, P. M. Remes, R. Huguet, G. McAlister, M. Goodwin, R. Viner, J. E. P. Syka, and C. V. Robinson, “Combining native and ‘omics’ mass spectrometry to identify endogenous ligands bound to membrane proteins,” *Nature Methods* **17**, 505–508 (2020).
- ⁵E. Christofi and P. Barran, “Ion mobility mass spectrometry (im-ms) for structural biology: Insights gained by measuring mass, charge, and collision cross section,” *Chem. Rev.* **123**, 2902–2949 (2023).
- ⁶S. A. Chandler and J. L. P. Benesch, “Mass spectrometry beyond the native state,” *Current Opinion in Chemical Biology* **42**, 130–137 (2018).
- ⁷H. M. Britt and C. V. Robinson, “Traversing the drug discovery landscape using native mass spectrometry,” *Current Opinion in Structural Biology* **91**, 102993 (2025).
- ⁸S. Rauschenbach, M. Ternes, L. Harnau, and K. Kern, “Mass spectrometry as a preparative tool for the surface science of large molecules,” *Annu Rev Anal Chem (Palo Alto Calif)* **9**, 473–98 (2016), rauschenbach, Stephan Ternes, Markus Harnau, Ludger Kern, Klaus eng Review 2016/04/19 *Annu Rev Anal Chem (Palo Alto Calif)*. 2016 Jun 12;9(1):473-98. doi: 10.1146/annurev-anchem-071015-041633. Epub 2016 Apr 21.
- ⁹J. L. P. Benesch, B. T. Ruotolo, D. A. Simmons, N. P. Barrera, N. Morgner, L. Wang, H. R. Saibil, and C. V. Robinson, “Separating and visualising protein assemblies by means of preparative mass spectrometry and microscopy,” *Journal of Structural Biology* **172**, 161–168 (2010).
- ¹⁰V. A. Mikhailov, T. H. Mize, J. L. P. Benesch, and C. V. Robinson, “Mass-selective soft-landing of protein assemblies with controlled landing energies,” *Analytical Chemistry* **86**, 8321–8328 (2014), doi: 10.1021/ac5018327.

- ¹¹T. K. Esser, J. Böhning, P. Fremdling, M. T. Agasid, A. Costin, K. Fort, A. Konijnenberg, J. D. Gilbert, A. Bahm, A. Makarov, C. V. Robinson, J. L. P. Benesch, L. Baker, T. A. M. Bharat, J. Gault, S. Rauschenbach, and J. Wand, “Mass-selective and ice-free electron cryomicroscopy protein sample preparation via native electrospray ion-beam deposition,” *PNAS Nexus* **1** (2022), 10.1093/pnasnexus/pgac153.
- ¹²M. S. Westphall, K. W. Lee, A. Z. Salome, J. M. Lodge, T. Grant, and J. J. Coon, “Three-dimensional structure determination of protein complexes using matrix-landing mass spectrometry,” *Nature Communications* **13**, 2276 (2022).
- ¹³M. S. Westphall, K. W. Lee, C. Hemme, A. Z. Salome, K. Mertz, T. Grant, and J. J. Coon, “Cryogenic soft landing improves structural preservation of protein complexes,” *Anal. Chem.* **95**, 15094–15101 (2023).
- ¹⁴T. K. Esser, J. Böhning, A. Önür, D. K. Chinthapalli, L. Eriksson, M. Grabarics, P. Fremdling, A. Konijnenberg, A. Makarov, A. Botman, C. Peter, J. L. P. Benesch, C. V. Robinson, J. Gault, L. Baker, T. A. M. Bharat, and S. Rauschenbach, “Cryo-em of soft-landed β -galactosidase: Gas-phase and native structures are remarkably similar,” *Science Advances* **10**, ead14628 (2024).
- ¹⁵H. Ochner, S. Szilagy, S. Abb, J. Gault, C. V. Robinson, L. Malavolti, S. Rauschenbach, and K. Kern, “Low-energy electron holography imaging of conformational variability of single-antibody molecules from electrospray ion beam deposition,” *Proceedings of the National Academy of Sciences* **118**, e2112651118 (2021).
- ¹⁶H. Ochner, S. Rauschenbach, and L. Malavolti, “Electrospray ion beam deposition plus low-energy electron holography as a tool for imaging individual biomolecules,” *Essays Biochem* **67**, 151–163 (2023).
- ¹⁷N. Vats, S. Rauschenbach, W. Sigle, S. Sen, S. Abb, A. Portz, M. Dürr, M. Burghard, P. A. van Aken, and K. Kern, “Electron microscopy of polyoxometalate ions on graphene by electrospray ion beam deposition,” *Nanoscale* **10**, 4952–4961 (2018).
- ¹⁸A. Punjani, J. L. Rubinstein, D. J. Fleet, and M. A. Brubaker, “cryosparc: algorithms for rapid unsupervised cryo-em structure determination,” *Nature Methods* **14**, 290–296 (2017).
- ¹⁹J. Zivanov, T. Nakane, B. O. Forsberg, D. Kimanius, W. J. H. Hagen, E. Lindahl, and S. H. W. Scheres, “New tools for automated high-resolution cryo-em structure determination in relion-3,” *eLife* **7**, e42166 (2018).
- ²⁰A. Walz, K. Stoiber, A. Huettig, H. Schlichting, and J. V. Barth, “Navigate flying molecular elephants safely to the ground: Mass-selective soft landing up to the mega-dalton range by

- electrospray controlled ion-beam deposition,” *Analytical Chemistry* **94**, 7767–7778 (2022), doi: 10.1021/acs.analchem.1c04495.
- ²¹P. Fremdling, T. K. Esser, B. Saha, A. A. Makarov, K. L. Fort, M. Reinhardt-Szyba, J. Gault, and S. Rauschenbach, “A preparative mass spectrometer to deposit intact large native protein complexes,” *ACS Nano* **16**, 14443–14455 (2022), fremdling, Paul Esser, Tim K Saha, Bodhisattwa Makarov, Alexander A Fort, Kyle L Reinhardt-Szyba, Maria Gault, Joseph Rauschenbach, Stephan eng 2022/08/30 *ACS Nano*. 2022 Sep 27;16(9):14443-14455. doi: 10.1021/acsnano.2c04831. Epub 2022 Aug 29.
- ²²C. Hamann, R. Woltmann, I.-P. Hong, N. Hauptmann, S. Karan, and R. Berndt, “Ultrahigh vacuum deposition of organic molecules by electrospray ionization,” *Review of Scientific Instruments* **82** (2011).
- ²³W. G. Baechler, “Cryopumps for research and industry,” *Vacuum* **37**, 21–29 (1987).
- ²⁴S. Tacke, P. Erdmann, Z. Wang, S. Klumpe, M. Grange, J. Plitzko, and S. Raunser, “A streamlined workflow for automated cryo focused ion beam milling,” *Journal of Structural Biology* **213**, 107743 (2021).
- ²⁵S. Abb, L. Harnau, R. Gutzler, S. Rauschenbach, and K. Kern, “Two-dimensional honeycomb network through sequence-controlled self-assembly of oligopeptides,” *Nature Communications* **7**, 10335 (2016).
- ²⁶S. Kahle, Z. Deng, N. Malinowski, C. Tonnoir, A. Forment-Aliaga, N. Thontasen, G. Rinke, D. Le, V. Turkowski, T. S. Rahman, S. Rauschenbach, M. Ternes, and K. Kern, “The quantum magnetism of individual manganese-12-acetate molecular magnets anchored at surfaces.” *Nano letters* **12**, 518–21 (2012).
- ²⁷L. A. Passmore, C. J. Russo, and R. A. Crowther, “Chapter three - specimen preparation for high-resolution cryo-em,” in *Methods in Enzymology*, Vol. 579 (Academic Press, 2016) pp. 51–86.
- ²⁸G. Weissenberger, R. J. M. Henderikx, and P. J. Peters, “Understanding the invisible hands of sample preparation for cryo-em,” *Nature Methods* **18**, 463–471 (2021).
- ²⁹J. P. McGee, R. D. Melani, P. F. Yip, M. W. Senko, P. D. Compton, J. O. Kafader, and N. L. Kelleher, “Isotopic resolution of protein complexes up to 466 kda using individual ion mass spectrometry.” *Analytical chemistry* **93**, 2723–2727 (2021).
- ³⁰P. Fremdling, *Preparative Mass Spectrometry Instrumentation for Large Native Protein Deposition*, Thesis, University of Oxford (2023).

- ³¹M. Barth, R. K. Bryan, and R. Hegerl, “Approximation of missing-cone data in 3d electron microscopy,” *Ultramicroscopy* **31**, 365–378 (1989).
- ³²K. Braig, Z. Otwinowski, R. Hegde, D. C. Boisvert, A. Joachimiak, A. L. Horwich, and P. B. Sigler, “The crystal structure of the bacterial chaperonin groel at 2.8 Å,” *Nature* **371**, 578–586 (1994).
- ³³S. V. Barrass, T. K. Esser, N. J. Mowry, L. Eriksson, J. Hruby, L. T. Seeley, M. Drabbels, L. A. Baker, S. Rauschenbach, and U. J. Lorenz, “An alternative cryo-em sample preparation workflow based on soft-landing and laser flash melting,” *In Preparation* (2025).
- ³⁴S.-H. Roh, C. F. Hryc, H.-H. Jeong, X. Fei, J. Jakana, G. H. Lorimer, and W. Chiu, “Subunit conformational variation within individual groel oligomers resolved by cryo-em,” *Proceedings of the National Academy of Sciences* **114**, 8259–8264 (2017).
- ³⁵T. Croll, “Isolde: a physically realistic environment for model building into low-resolution electron-density maps,” *Acta Crystallographica Section D* **74**, 519–530 (2018).
- ³⁶L. H. Urner, “Advances in membrane mimetics and mass spectrometry for understanding membrane structure and function,” *Current Opinion in Chemical Biology* **69**, 102157 (2022).
- ³⁷A. Oluwole, D. Shutin, and J. Bolla, “Mass spectrometry of intact membrane proteins: shifting towards a more native-like context,” *Essays Biochem* **67**, 201–213 (2023).
- ³⁸U. Flores-Perez and P. Jarvis, “Isolation and suborganellar fractionation of arabidopsis chloroplasts.” *Methods in molecular biology (Clifton, N.J.)* **1511**, 45–60 (2017).
- ³⁹E. F. Pettersen, T. D. Goddard, C. C. Huang, E. C. Meng, G. S. Couch, T. I. Croll, J. H. Morris, and T. E. Ferrin, “Ucsf chimeraX: Structure visualization for researchers, educators, and developers,” *Protein Science* **30**, 70–82 (2021).
- ⁴⁰D. N. Mastrorade, “Automated electron microscope tomography using robust prediction of specimen movements.” *Journal of structural biology* **152**, 36–51 (2005).
- ⁴¹J. R. Kremer, D. N. Mastrorade, and J. R. McIntosh, “Computer visualization of three-dimensional image data using imod.” *Journal of structural biology* **116**, 71–6 (1996).
- ⁴²D. Necas and P. Klapetek, “Gwyddion: an open-source software for SPM data analysis,” *Central European Journal of Physics* **10**, 181–188 (2012).